Ore Geology Reviews 145 (2022) 104909

Contents lists available at ScienceDirect

Ore Geology Reviews

journal homepage: www.elsevier.com/locate/oregeorev

Skarn classification and element mobility in the Yeshan Iron Deposit, Eastern China: Insight from lithogeochemistry

Shugao Zhao [a,*], Matthew J. Brzozowski [b], Thomas Mueller [c], Lijuan Wang [d], Weiqiang Li [a,*]

[a] State Key Laboratory for Mineral Deposits Research, School of Earth Sciences and Engineering, Nanjing University, Nanjing 210046, China
[b] Department of Geology, Lakehead University, Thunder Bay, Ontario, Canada, P7B 5E1
[c] Geoscience Center, Georg-August-University Göttingen, D-37077 Göttingen, Germany
[d] Geological Survey of Jiangsu Province, Nanjing 210018, Jiangsu, China

ARTICLE INFO

Keywords:
Mass exchange
Skarn alteration
Bulk-rock geochemistry
Protolith

ABSTRACT

Skarns form by significant fluid-mediated exchange of mass and heat between igneous rocks and their surrounding wall rocks into which they intruded. Quantification of the mass exchange associated with skarn alteration requires knowledge of the skarn protoliths, which are often masked by metamorphic recrystallization and intense calc-silicate metasomatism. To overcome this challenge in characterizing the Yeshan skarn Fe deposit in Eastern China, a cross-section through the complete rock sequence, from the carbonate wall rock to the pluton, was systematically sampled, and analyzed for bulk-rock major and trace elements. Underpinned by the skarn zonation model, $\ln(SiO_2/Al_2O_3)$, $\ln(SiO_2/TiO_2)$, and REE + Y values in the skarns were used to distinguish the various skarn protoliths. The effectiveness of the $\ln(SiO_2/Al_2O_3)$ and $\ln(SiO_2/TiO_2)$ is supported by the variable mobility of Si, Al, and Ti during magma-derived fluid infiltration into the carbonate wall rocks at Yeshan. The effectiveness of REE + Y is based on their significant concentration differences in the carbonate wall rocks and igneous rocks at Yeshan. These geochemical indexes may be applicable to the characterization of protoliths and mass transfer in skarn deposits where igneous rocks intruded carbonate wall rocks.

1. Introduction

Skarns are the product of metasomatic processes that result in a substantial amount of heat and mass exchange between igneous rocks and wall rocks in the presence of hydrothermal fluids. Based on the characteristics of the protolith, skarns can be divided into endoskarns and exoskarns, which correspond to skarns developed in the igneous rocks and the wall rocks, respectively (Einaudi et al., 1981; Meinert et al., 2005).

With respect to skarn deposit exploitation, determination of the protoliths is essential to mineral resource estimation. It is also of economic significance for metallurgy because grinding efficiency, liberation characteristics, and metal recovery are affected by the mineral assemblages and particle size distribution, both of which are closely linked to primary lithological characteristics (e.g., Maydagán et al., 2016). Identification of the protolith is quite challenging, however, as intense thermal metamorphism and calc-silicate metasomatism can completely mask the primary textures of the protolith (e.g., Mrozek et al., 2020; Ordóñez-Calderón et al., 2017). Mrozek et al, (2020) demonstrated that immobile elements, including Al_2O_3, heavy rare elements, and some high field strength elements, could be used to classify exoskarns and endoskarns at the Antanima Cu-Zn skarn system. However, these elements have been shown to be mobile at other skarn deposits (Gieré, 1990; Lentz, 2005, and references therein), as well as the Yeshan skarn Fe deposit in this study. Characterization of the protolith in the Yeshan skarn Fe deposit, therefore, poses unique challenges and requires a geological–geochemical toolset that is different from that applied to the Antanima Cu-Zn skarn system.

Our study reveals that underpinned by the skarn zonation model, SiO_2/Al_2O_3, SiO_2/TiO_2 and REE + Y contents could be used to distinguish the various skarn protoliths at the Yeshan skarn Fe deposit. Additionally, the gains and losses of elements associated with the skarn development at Yeshan are quantified.

2. Geologic setting

The Middle–Lower Yangtze River metallogenic belt (MLYB), covering an area of about 108,000 km^2, is bounded by three major faults

* Corresponding authors.
E-mail addresses: zhaoshugao@smail.nju.edu.cn (S. Zhao), liweiqiang@nju.edu.cn (W. Li).

https://doi.org/10.1016/j.oregeorev.2022.104909
Received 17 November 2021; Received in revised form 19 April 2022; Accepted 20 April 2022
Available online 26 April 2022
0169-1368/© 2022 The Author(s). Published by Elsevier B.V. This is an open access article under the CC BY license (http://creativecommons.org/licenses/by/4.0/).

— the Tangcheng–Lujiang Fault (TLF) in the northwest, the Xiangfan–Guangji Fault (XGF) in the southwest, and the Yangxin–Changzhou Fault (YCF) in the south (Fig. 1). It is adjacent to the Yangtze craton, the North China craton, and the Qinling–Dabieshan orogenic belt (Fig. 1). The MLYB is one of the most important Cu–Fe–Au–Mo–Pb–Zn–W polymetallic provinces in Eastern China (Mao et al., 2011a). Systematic research on this area dates back to the 1920s, and major reviews include Chang et al., (1991), Zhai et al., (1992), Pan and Dong (1999), and Pirajno (2013). It hosts more than 200 mineral deposits that have been clustered into seven ore districts — Edong, Jiurui, Anqing–Guichi, Luzong, Tongling, Ningwu, and Ningzhen (Fig. 1).

Two main groups of mineral deposits are recognized in the MLYB according to their tectonic, magmatic, and mineralization characteristics (Mao et al., 2011b). (1) Porphyry–skarn–stratabound Cu–Au–Mo deposits (148–135 Ma) in fault uplifted regions; they are genetically related to I-type, high-K, calc-alkaline granitoids, with high Sr/Y ratios typical of adakitic rocks (156–137 Ma). (2) Magnetite–apatite deposits (135–123 Ma) in rift basins, which are associated with similarly aged calc-alkaline igneous rocks and their corresponding shoshonitic extrusive equivalents. Recently, the magnetite-apatite mineralization (~130 Ma) has also been identified in the volcanic basin within the Edong ore district (Hu et al., 2020), the geological characteristics (e.g., the volcanic sequences and the tectonic setting) of which are similar to the Ningwu and Luzong volcanic basins (Mao et al., 2011b; Ningwu Research Group, 1978; Zhou et al., 2013). Other types of mineral deposits in the region include porphyry–skarn–stratabound Cu–Au–Mo deposits that are younger than 135 Ma (Deng et al., 2016; Liang et al., 2018), skarn Fe–Cu deposits (e.g., Xie et al., 2011; Li et al., 2014), Fe-only skarn deposits, including the Chengchao, Jinshandian, Longqiao and Yeshan deposits (Fig. 1; Zhou et al., 2011; Xie et al., 2012; Chen et al., 2018), and a small number of Cu–Au-bearing hydrothermal veins (Fan et al., 2008; Yu et al., 2016).

The Ningzhen ore district, situated in the easternmost part of the MLYB (Fig. 1), contains numerous deposits enriched in Pb, Zn, Ag, Cu, Fe, and Mo (Fig. 2). The Ningzhen ore district comprises mainly three tectonostratigraphic units — Mesoproterozoic metamorphic basement, Sinian–Triassic sedimentary cover, and Jurassic–Neogene superimposed cover. The basement rock is the unexposed Picheng Group, which comprises schists, amphibolites, and granulites, with a total thickness of more than 480 m (Jiangsu Bureau Geological Mineral Resource, 1989). The overlying Sinian–Triassic sedimentary rocks comprise marine carbonate, and terrestrial shale and siltstone. The Sinian–Triassic carbonate rocks are closely related to most of the mineral deposits in the ore district, including the Qixiashan Pb–Zn–Ag, Anjishan Cu, Tongshan Cu, Weigang Fe, Jianbi Mo, and Yeshan Fe deposits (Fig. 2). The Sinian–-Triassic sedimentary rocks were strongly folded in the middle Triassic by the Indosinian Orogeny. The axial lines of these folds strike northeast in the western segment of the Ningzhen ore district, but change to a more dominant east–west strike in the central portion of the district (Fig. 2). Prior to the Jurassic, the Ningzhen ore district became an active continental margin (e.g., Zhou and Li, 2000; Li and Li, 2007).

The Early Jurassic sediments are characterized by a terrestrial succession of conglomerate, sandstone, and mudstone, and are mainly distributed in the eastern portion of Ningzhen ore district (Fig. 2). From the Late Jurassic to the Cretaceous, it has generally been accepted that this continental margin was influenced by the westward subduction of the Pacific plate and the Izanagi plate (e.g., Ling et al., 2009), with a series of NNE-, NNW-, NE- and EW-trending faults having formed and superimposed on the folds in the ore district (Fig. 2). The plate subduction event was also a trigger for the intrusion of large volumes of granitoids and the eruption of volcanic rocks. There are seven 110–100 Ma quartz diorite–granodiorite–granite intrusions exposed in the middle segment of the ore district (Zeng et al., 2013; Chen et al., 2017; Zhang et al., 2018); from west to east these are the Bancang, Qilinmen, Anjishan, Xiashu–Gaozi, Xinqiao, Shima, and Jianbi intrusions (Fig. 2) (Sun et al., 2013). The Yeshan intrusion, which is the focus of this study,

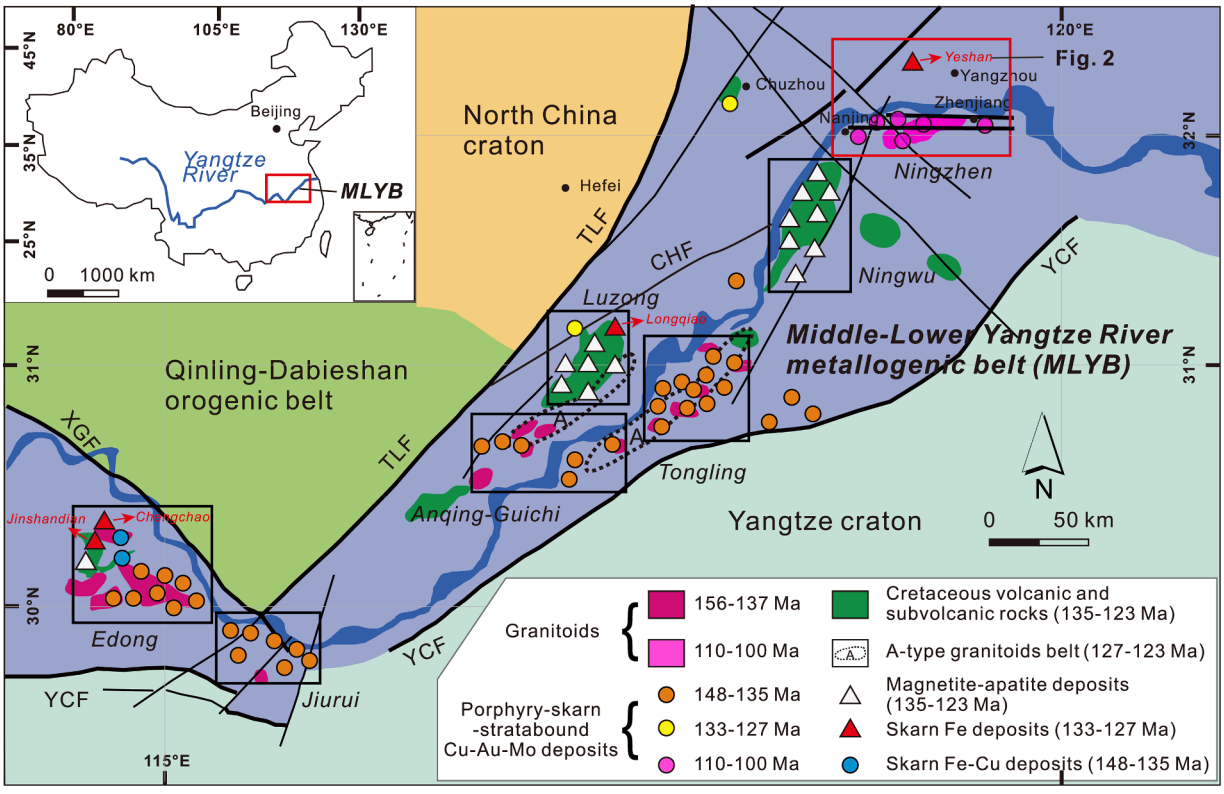

Fig. 1. Geologic map showing the distribution of porphyry–skarn–stratabound Cu–Au–Mo, skarn Fe–Cu, skarn Fe, and magnetite-apatite deposits along with the Middle–Lower Yangtze River metallogenic belt (modified after Pan and Dong, 1999; Mao et al., 2011a; Mao et al., 2011b; Li et al., 2019; Hu et al., 2020; Xiao et al., 2021). Abbreviations: XGF = Xiangfan–Guangji Fault; TLF = Tancheng–Lujiang Fault; YCF = Yangxin–Changzhou Fault; CHF = Chuhe Fault.

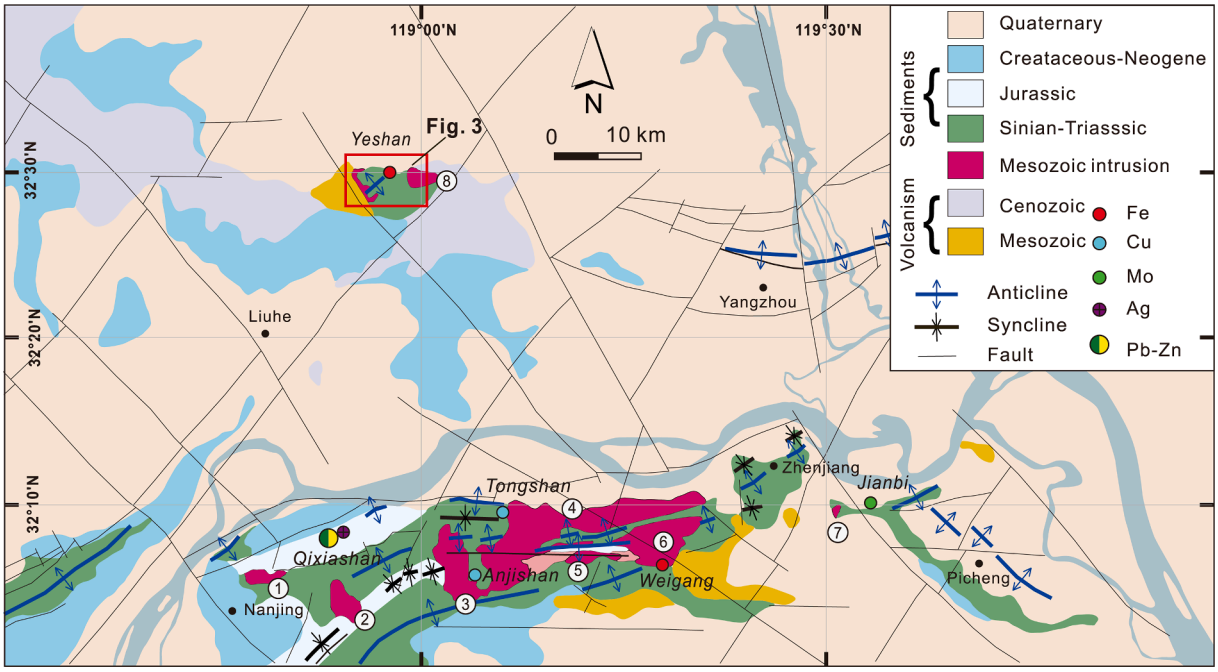

Fig. 2. Geologic map of the Ningzhen ore district showing the locations of major deposits, including Qixiashan Pb–Zn–Ag, Anjishan Cu, Tongshan Cu, Weigang Fe, Jianbi Mo, and Yeshan Fe deposits. The numbers represent the Mesozoic intrusions: 1 = Bancang, 2 = Qilinmen, 3 = Anjishan, 4 = Xiashu-Gaozi, 5 = Xinqiao, 6 = Shima, 7 = Jianbi, 8 = Yeshan intrusions, respectively.

is located in the northernmost portion of the Ningzhen ore district and has a zircon U–Pb age of 128 Ma (Chen et al., 2018), suggesting that it crystallized from a different magmatic pulse than those from which the other intrusions in the Ningzhen ore district formed (Fig. 2).

3. Deposit geology

The Yeshan skarn Fe deposit is located about 20 km northeast of Liuhe City, Jiangsu Province (Fig. 2). The ore field is located proximal to the Jiangpu–Liuhe fault (JLF) to the southeast and the Tianchang–Yizheng fault (TYF) to the southwest (Fig. 3). The Yeshan deposit was initially produced as an open-pit mine, but began underground production in 1971. With an iron ore reserve of 23.7 million tons (Mt) as of 2015 (Yeshan Mining Co. Ltd., unpublished report), the deposit represents an important source of iron in the Ningzhen ore district. Although the Yeshan deposit is, by definition, a classic example of Fe skarn mineralization, no systematic geological or geochemical studies of the deposit have been published. Literature pertinent to the deposit are in Chinese and mostly pertain to the genesis of the pluton (Zi et al., 2011; Chen et al., 2018). Discussions on the mineralization mechanisms are elusive (Sun et al., 2017).

The deposit comprises three ore zones — the North, Eastern, and Tieshigang ore zones (Fig. 3) — and contains nine major tabular- and lens-shaped economic ore bodies that occur within the pluton (in the case of the Tieshigang ore zone) or at the contact zone between the pluton and the wall rock (in the case of the North and Eastern ore zones). The individual ore bodies have thicknesses of 0.55–54.7 m and lengths of 10–320 m. In the North ore zone, the ore bodies strike northwest, dip at 25–65° to the southwest, and contain average Fe and Cu grades of approximately 44.24 wt% and 0.40 wt%, respectively. In the Eastern ore zone, Fe ore bodies strike east–west and dip at 40–75° to the south, with an average Fe grade of 37.58 wt%. The Eastern ore zone also contains B mineralization hosted by camsellite and ludwigite, with a reserve of 280,000 tons at an average ore grade of 11.32 wt%. No Cu mineralization exists in the Eastern zone. In the Tieshigang ore zone, Fe ore bodies strike northeast and dip at 75–85° to the southeast, and contain average Fe and Cu grades of approximately 42.09 wt% and 0.15 wt%, respectively. The ore-bearing pluton at Yeshan can be subdivided into three facies based on petrographic and geochemical characteristics (Fig. 3) — granodiorite in the eastern portion, diorite in the western and southeastern portions, and quartz monzonite in the central portion. Zircon U–Pb dating yields ages of 128 ± 2 Ma and 129 ± 2 Ma for the granodiorite and southeastern diorite, respectively (Chen et al., 2018).

The wall rocks of the Yeshan deposit are controlled by NNW- and NE-trending faults (Fig. 3). The ore-related wall rocks comprise Sinian and lower Cambrian strata that are separated by four nearly parallel thrust faults (Fig. 3). The Sinian Huangxu Formation is mainly composed of limestone and dolomitic limestone. It is uncoformably overlain by the Dengying Formation, which consists of a dark grey dolostone intercalated with siliceous and muddy layers. The lower Cambrian strata, including the Hetang and Mufushan formations, unconformably overly the Sinian Dengying Formation. The Hetang Formation is characterized by black carbonaceous and/or siliceous shale, whereas the Mufushan Formation consists predominantly of dolomite intercalated with silicified hornfels.

Other wall rocks are unrelated to skarn mineralization in the Yeshan deposit, and include Jurassic and Cretaceous strata (Fig. 3; Chen et al., 2018). The Jurassic Xihengshan Formation is composed of quartz sandstone intercalated with thin layers of siltstone. The Jurassic Longwangshan Formation is a suite of pyroclastic rocks containing andesite intercalated with mudstone and tuff. The Cretaceous Pukou Formation consists of packsand, siltstone, and silty mudstone. The Cretaceous Chishan Formation comprises quartz sandstone, siltstone, and mudstone (Chen et al., 2018).

4. Samples and analytical techniques

Samples selected for this study were taken from drill core ZK302 at the Xiaomiaochen area of the Yeshan deposit (Fig. 4a), which is to the northern of the North ore zone (Fig. 3). The drill core extends to a depth of ~900 m and intersects a complete sequence of rocks that make up the deposit, from the carbonate wall rock, skarn, to the igneous pluton. More than 60 samples were collected along the length of the drill core at intervals of approximately 20 m (Fig. 4b).

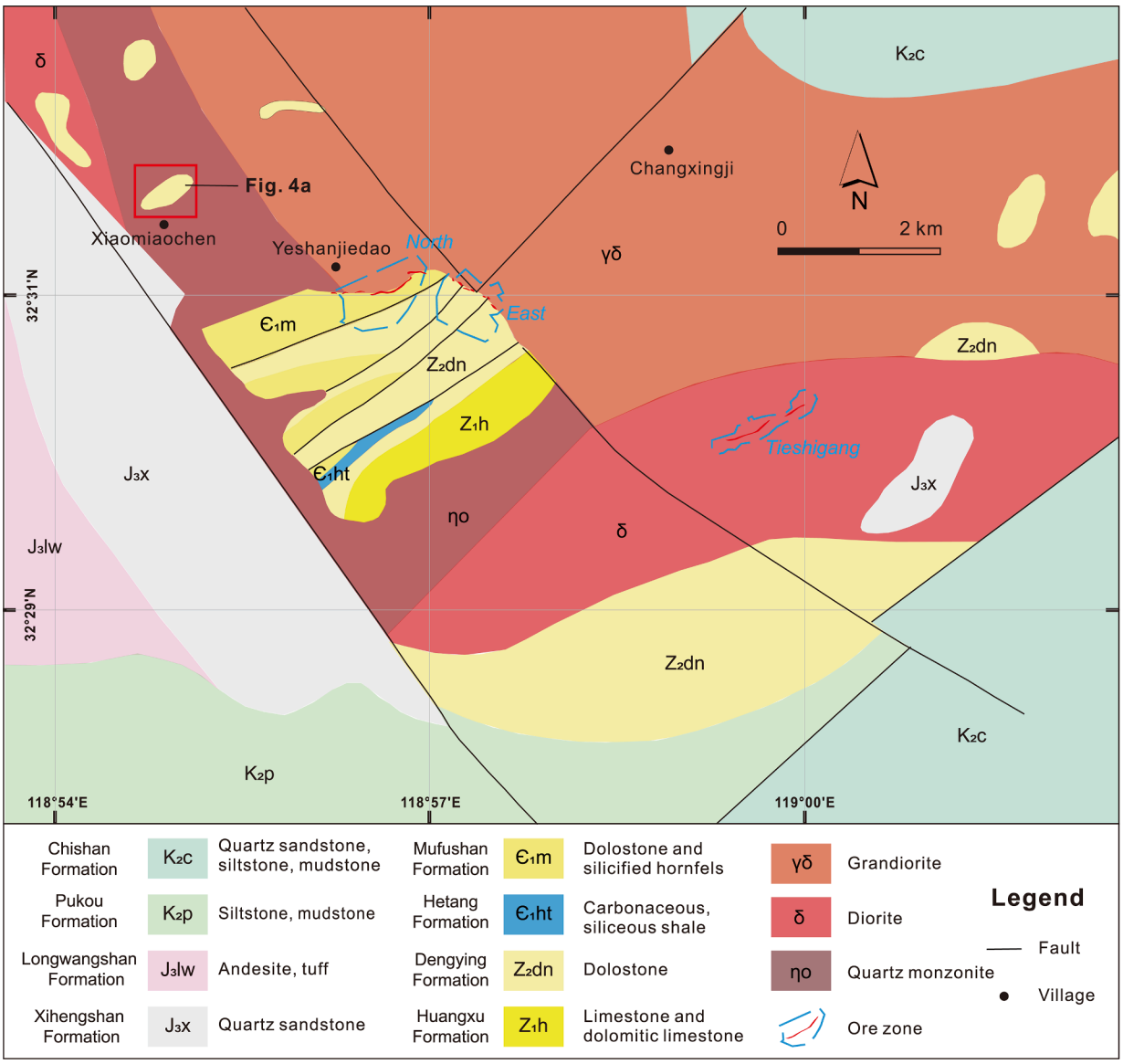

Fig. 3. Geologic map of the Yeshan Fe deposit showing the distribution of orebodies.

4.1. Whole-rock geochemistry

The major-element composition of the skarns (n = 21) and quartz monzonite (n = 15) was determined using a Thermo Scientific ARL-9900 X-ray fluorescence spectrometer (XRF) at the State Key Laboratory for Mineral Deposits Research, Nanjing University. Prior to XRF analyses, rock powders were heated for 4 h at 105 °C to remove pore and surface water. The whole-rock powders (1.0 g) were then mixed with $Li_2B_4O_7$ + $LiBO_2$ + LiBr (11 g) and fused into glass disks. Loss on ignition (LOI) was determined by changes in the weight of the samples after being heated at 1050 °C for 3 h. Reference materials GBW–07103, GBW–07135, BHVO–2, and BCR–2 were used as external standards to monitor analytical accuracy. Analytical precision for major elements is better than 2%. The major-element composition of marbles (n = 14) was measured by a PANalytical Magix Fast XRF using the ME-XRF26 package at ALS Chemex Co., Ltd (Guangzhou, China). Analytical uncertainty is better than 5%. The trace-element composition of the skarns (n = 21), quartz monzonite (n = 15), and marbles (n = 14) was determined by a Perkin Elmer Elan-9000 inductively coupled plasma mass spectrometry (ICP–MS) using the ME-MS81 package at ALS Chemex (Guangzhou). A prepared whole-rock power was added to lithium borate flux ($LiBO_2$/$Li_2B_4O_7$), mixed well, and fused in a furnace at 1025 °C. After cooling, the melt was dissolved in the HCl-HNO_3-HF mixture for analysis. Analytical precision and accuracy monitored by USGS rock standards (BCR-2, BHVO-1 and AGV-1) is better than 10%.

4.2. Isocon analysis

Mass transfer caused by hydrothermal alteration can be quantified by comparing the bulk chemical composition of original and altered rocks. The graphical isocon method of Grant (1986) is used here to investigate element mobility during skarn formation. The basic equation for the isocon method is.

$$C_i^A = (M^O/M^A) * (C_i^O + \Delta C_i)$$

where C_i^A and C_i^O represent the concentration of element i in altered and original rocks, respectively, and M^A and M^O denote the total mass of the altered and original rocks, respectively. The slope of the isocon line is defined by M^O/M^A. The gain or loss of element i is given by.

$$\Delta C_i/C_i^O = (M^A/M^O) * (C_i^A/C_i^O) - 1$$

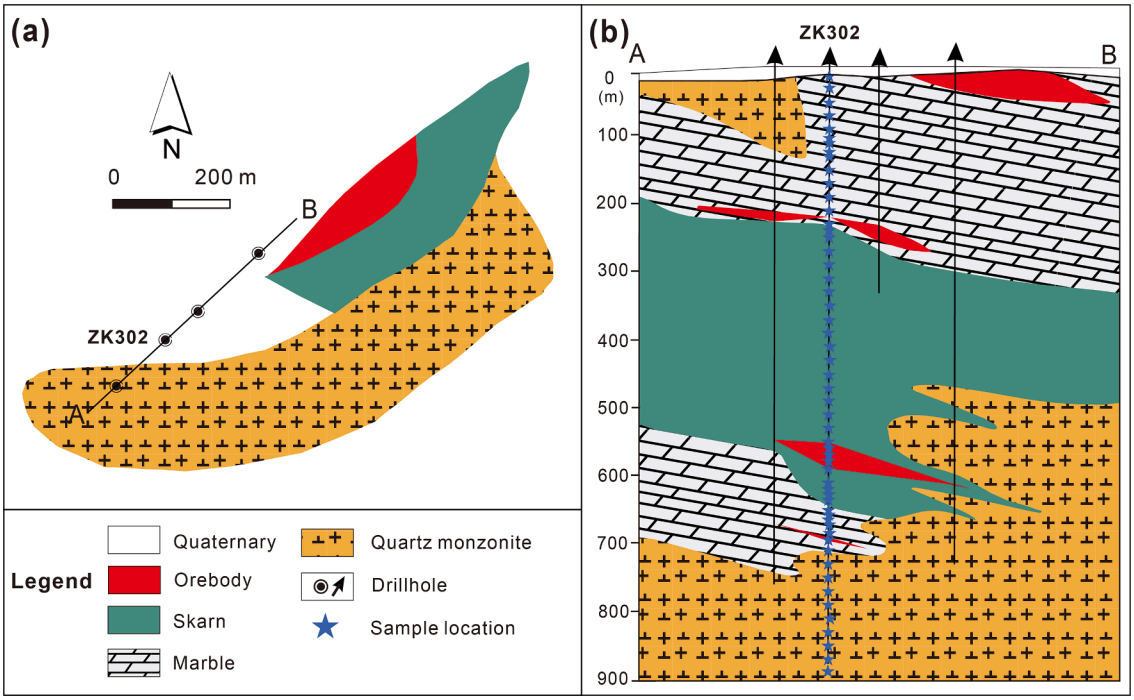

Fig. 4. (**a**) Geological map of the Xiaomiaochen area. (**b**) Cross-section A–B showing the spatial relationship among the marble, the intrusion, the skarns, and the orebodies in the Yeshan deposit, as well as the location of samples used in the study.

Given that the magnitude of numeric values varies among elements, the geochemical data of original and altered rocks are artificially scaled for portrayal in the isocon diagram. Elements are divided into two groups by the isocon line. Elements plotting above the isocon line were gained during the hydrothermal alteration, while those plotting below the isocon line were lost.

5. Results

5.1. Petrography

Fig. 5 schematically illustrates the lithological variations in drill hole ZK302. The lithological zones include, from top to bottom, dolomite marble, brucite marble, serpentinized marble, diopside skarn, garnet skarn, garnet–diopside skarn, epidote skarn, the ore body, serpentinized marble, chloritized quartz monzonite, and quartz monzonite (Fig. 5). Of the different types of skarn, garnet skarn is the most abundant. Dolomite marble predominantly comprises dolomite (>90 vol%), with an average grain size of >200 μm. Apatite in dolomite marbles occurs as 100–400 μm, euhedral–subhedral, elongate–granular crystals (Fig. 5a). Brucite marble mainly consists of calcite, brucite, and dolomite in varying proportions. Brucite, which makes up 10–30% of the rock by volume, occurs as oval-shaped grains that are 100–400 μm in diameter (Fig. 5b). Serpentinized marble is characterized by the presence of serpentine, which coexists with phlogopite (Fig. 5c).

Diopside skarn predominantly comprises fine-grained (<200 μm), euhedral–subhedral diopside, lesser amounts of interstitial magnetite, and minor apatite, ilmenite, and Zr–Ti-bearing minerals (Fig. 5d, 6a). Garnet skarn is dominated by anisotropic, euhedral–subhedral garnet (Fig. 5e, f). Aggregates of garnet can be surrounded and infilled by quartz (Fig. 5e), can be isolated from quartz (Fig. 5f), or can be replaced by epidote (Fig. 6b). The grain size of garnet in garnet skarn varies in different locations. Generally, garnet skarn that occurs at depths of 290–330 m are dominated by fine-grained (<200 μm) garnet crystals (Fig. 5e, 6b), whereas garnet skarns that occur at a depth of ~390 m are dominated by coarse-grained (>500 μm) garnet crystals (Fig. 5f). Garnet–diopside skarn is largely composed of diopside, with subordinate garnet (Fig. 5g). Diopside occurs as euhedral–subhedral grains (100–300 μm in diameter) that are partially enclosed by garnet (Fig. 5g). In backscattered electron (BSE) images, diopside grains are homogeneous (i.e., no zonation) and are surrounded by zoned garnet, characterized by a bright rim and dark core (Fig. 6c). Epidote skarn is mainly composed of epidote, with some titanite inclusions (Fig. 5h, 6d). Epidote grains are euhedral–subhedral and range in size from 100 μm to >500 μm (Fig. 5h), while titanite grains are subhedral–anhedral and range from 50 to 150 μm in size (Fig. 6d). Other minerals recognized in epidote skarn, but which occur in low abundance, include quartz, calcite, apatite, chlorite, diopside, garnet, K-feldspar, and sulfide.

Magnetite, garnet, diopside, and epidote are the main constituents of the ore body at Yeshan (Fig. 5i), with magnetite being the main ore mineral and chalcopyrite being a minor component. Magnetite can also be associated with retrograde minerals, such as actinolite, in some of the ore-bearing skarns (Fig. 6e). Serpentinized marble also exists at a depth of ~650 m. Serpentinized marble here contains minor olivine crystals, which are surrounded by serpentine (Fig. 5j).

Skarn-altered quartz monzonite in which magmatic textures are preserved (e.g., coexistence of biotite and diopside) is locally recognized (Fig. 5k, 6f). In some skarn-altered quartz monzonite samples, biotite is partially replaced by chlorite (Fig. 6g). Adjacent to the skarn-altered quartz monzonite is the garnet–diopside skarn (Fig. 5l), in which some spinel and diopside grains are surrounded by phlogopite (Fig. 6h). Beneath the garnet–diopside skarn, a thin layer of ore-bearing phlogopite–serpentine skarn occurs (Fig. 6i).

Chlorite alteration is common in the quartz monzonite, and largely occurs as a replacement of hornblende (Fig. 5m). Quartz monzonite, which is light grey and coarse- to medium-grained, comprises plagioclase (25–40 vol%), amphibole (20–30 vol%), K-feldspar (15–25 vol%), quartz (10–20 vol%), and biotite (5–10 vol%) (Fig. 5n). Accessory minerals include zircon, titanite, apatite, and magnetite.

5.2. Geochemistry

The concentration of major elements, trace elements, and rare earth elements (REE) in samples from drill hole ZK302 are listed in Appendix

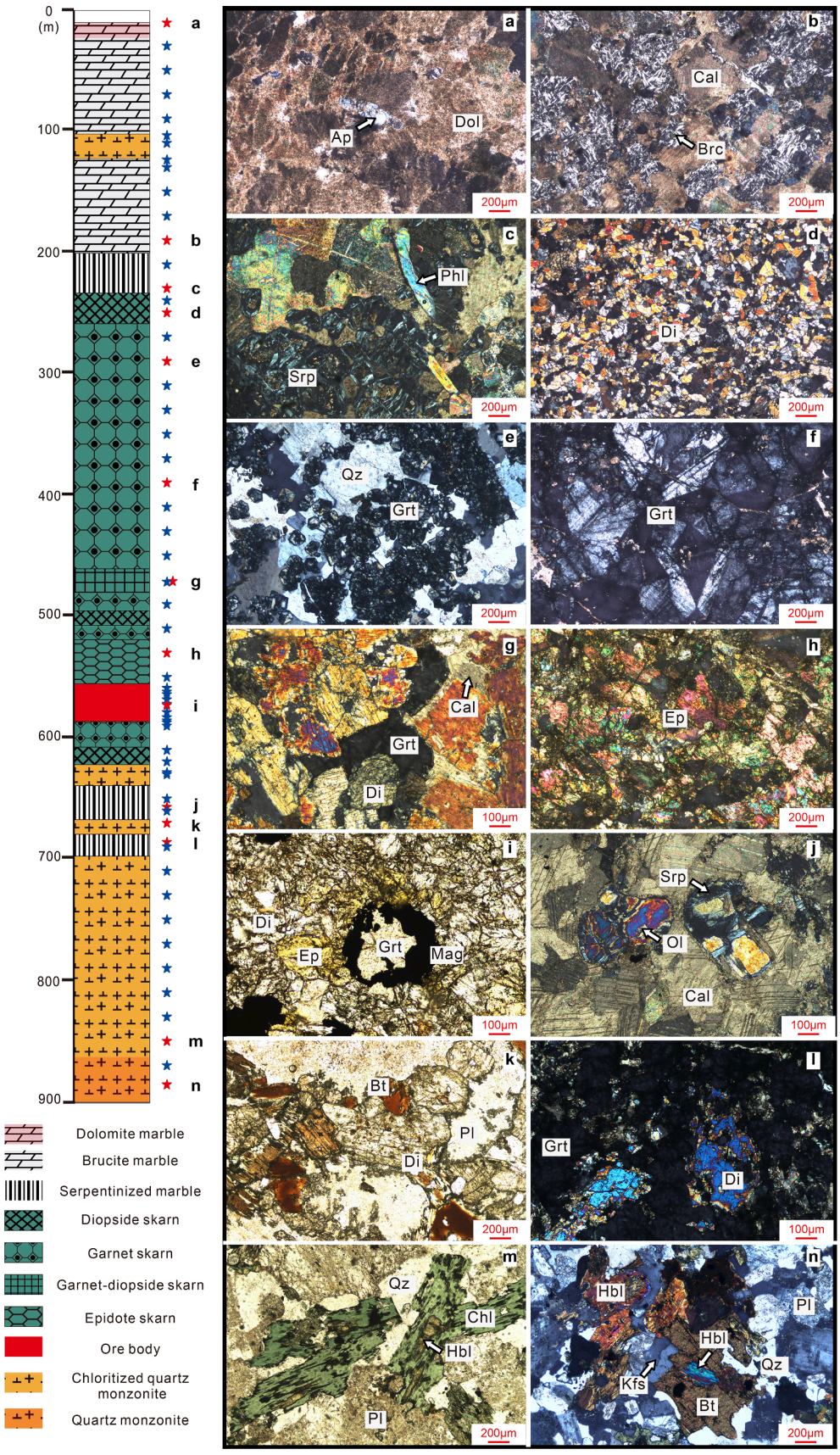

Fig. 5. Schematic column showing the lithological zones in drill hole ZK302, along with photomicrographs of the main lithologies in the Yeshan deposit. With increasing depth, the main lithological zones are distributed as dolomite marble, brucite marble, serpentinized marble, diopside skarn, garnet skarn, garnet–diopside skarn, epidote skarn, the ore body, serpentinized marble, chloritized quartz monzonite, and quartz monzonite. **(a–h, j, l, n)** Cross-polarized light images. **(i, k, m)** Plane-polarized light images. **(a)** Dolomite marble representing the least altered example of marine dolostone of Dengying Formation (ZK302-11). **(b)** Brucite marble (ZK302-190). **(c)** Serpentinized marble (ZK302-230). **(d)** Diopside skarn exhibiting a fine-grained equigranular texture (ZK302-250). **(e)** Garnet skarn with fine-grained garnet and interstitial quartz (ZK302-290). **(f)** Coarse-grained garnet skarn with calcite veinlets (ZK302-390). **(g)** Garnet–clinopyroxene skarn with diopside that has been replaced by garnet (ZK302-471). **(h)** Epidote skarn (ZK302-530). **(i)** Ore-bearing skarn comprising garnet, epidote, diopside, and magnetite (ZK302-568.3). **(j)** Serpentinized marble with forsterite replaced by serpentine (ZK302-657). **(k)** Skarn-altered quartz monzonite with plagioclase and biotite replaced by diopside (ZK302-670). **(l)** Garnet–diopside skarn with diopside enclosed by garnet (ZK302-686). **(m)** Chloritized quartz monzonite with hornblende replaced by chlorite (ZK302-850). **(n)** Quartz monzonite consisting of plagioclase, K-feldspar, hornblende, biotite, and quartz (ZK302-886). Mineral abbreviations (after Whitney and Evans, 2010): Ap = apatite, Brc = brucite, Bt = biotite, Cal = calcite, Chl = chlorite, Di = diopside, Dol = dolomite, Ep = epidote, Grt = garnet, Hbl = hornblende, Kfs = K-feldspar, Mag = magnetite, Ol = olivine, Phl = phlogopite, Pl = plagioclase, Qz = quartz, Srp = serpentine.

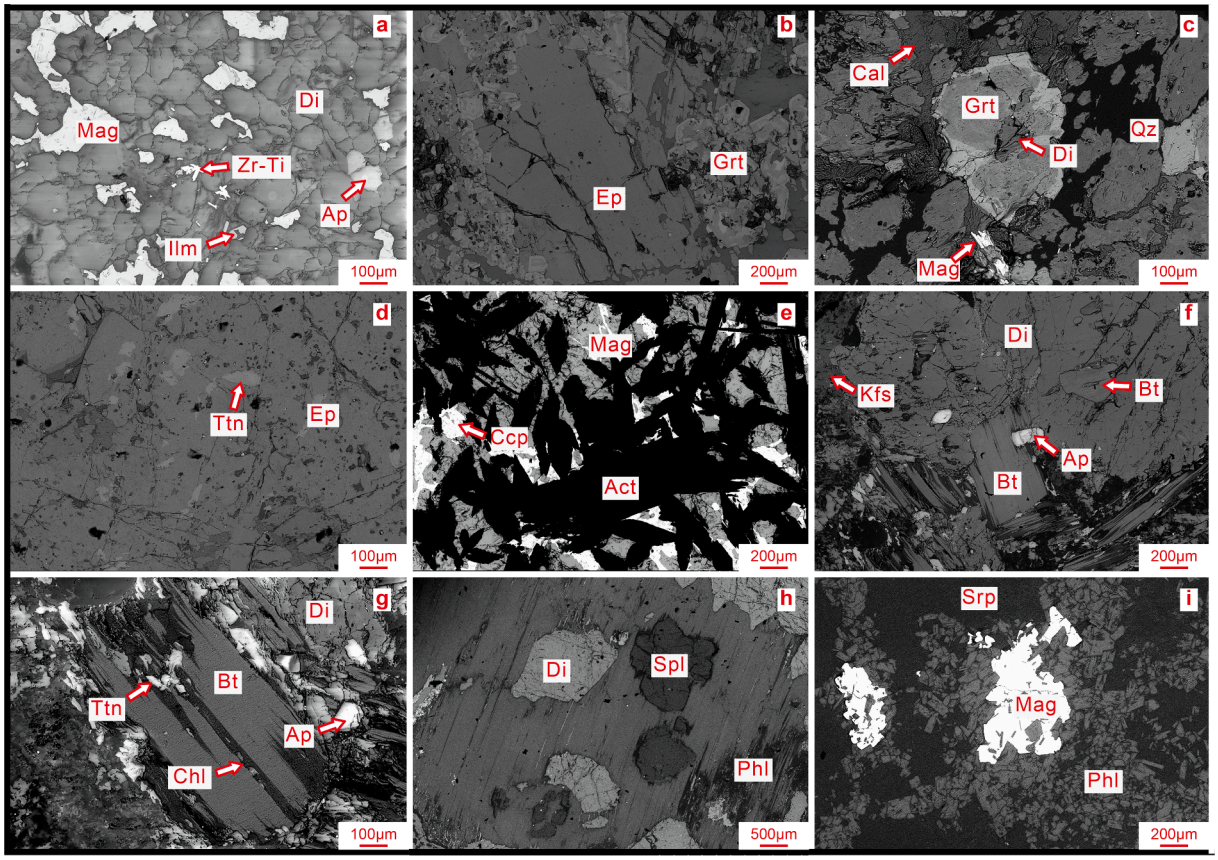

Fig. 6. Representative backscattered electron (BSE) images illustrating mineral assemblages and textural features in the Yeshan Fe deposit. (**a**) Magnetite filling the interstices of diopside grains, with minor apatite, ilmenite and a Zr–Ti-bearing mineral (ZK302-240). (**b**) Aggregate of garnet replaced by a large epidote crystal (ZK302-330). (**c**) Diopside enclosed by garnet that has a dark Fe-poor core and bright Fe-rich rim (ZK302-471.5). (**d**) Cluster of titanite inclusions in epidote (ZK302-530). (**e**) Actinolite intergrown with magnetite, which is crosscut by chalcopyrite (ZK302-619.7). (**f**) Diopside that has partially replaced K-feldspar. Note the sharp boundary between biotite and diopside (ZK302-670). (**g**) Biotite that has been replaced by chlorite, with newly formed titanite being distributed along the cleavage and margins of biotite (ZK302-670). (**h**) Phlogopite that has partially replaced replace fine-grained clinopyroxene and spinel (ZK302-686). (**i**) Coexisting magnetite, serpentine, and phlogopite (ZK302-690). Mineral abbreviations (after Whitney and Evans, 2010): Act = actinolite, Ap = apatite, Bt = biotite, Cal = calcite, Ccp = Chalcopyrite, Chl = chlorite, Di = diopside, Ep = epidote, Grt = garnet, Ilm = ilmenite, Kfs = K-feldspar, Mag = magnetite, Phl = phlogopite, Qz = quartz, Spl = spinel, Ttn = titanite, Zr-Ti = Zr–Ti-bearing mineral.

Table A. A comparison of the composition of marbles, skarns, and quartz monzonite is provided in Fig. 7.

The CaO and MgO concentrations, and LOI of the dolomite marble are 31.2 wt%, 20.7 wt%, and 46.6 wt%, respectively (Appendix Table A), which are similar to near-pure dolostone. Compared to dolomite marble, brucite marble has slightly higher CaO and MgO, but lower LOI (Fig. 7d–f). The CaO, MgO and LOI contents in serpentinized marble are similar to or slightly lower than dolomite marble and brucite marble (Fig. 7d-f). Serpentinized marble has higher SiO_2 contents than dolomite marble and brucite marble (e.g., Fig. 7a), consistent with its greater abundance of SiO_2-bearing minerals, such as serpentine, olivine, and phlogopite.

Quartz monzonite has a high-K calc-alkaline geochemical affinity based on the SiO_2–K_2O division of Peccerillo and Taylor (1976). Relative to the marbles, the quartz monzonite has higher SiO_2, TiO_2, Al_2O_3, and K_2O, but significantly lower CaO, MgO, and LOI contents (Fig. 7a–f). The quartz monzonite and marbles contain similar MnO and P_2O_5 concentrations, although few marble samples extend to higher concentrations (Fig. 7h, i). Major elements in the chloritized quartz monzonite exhibit a wider range of concentrations than unaltered quartz monzonite, with TiO_2, Al_2O_3, K_2O, Fe_2O_3, and MnO exhibiting the largest variations (Fig. 7a–i). Skarn-altered quartz monzonite has lower concentrations of SiO_2 and Fe_2O_3, and higher concentrations of TiO_2, CaO, MgO, LOI, and MnO than unaltered quartz monzonite.

Skarns have SiO_2 contents intermediate to the marbles and quartz monzonite, except for one garnet skarn sample (ZK302-290), which has a SiO_2 content of 60.8 wt% due to a greater abundance of quartz in this sample. The concentration of TiO_2 in skarns is highly variable (Fig. 7a). Epidote skarn has the highest TiO_2 contents, whereas diopside skarn and phlogopite–serpentine skarn have the lowest TiO_2 contents. Garnet–diopside skarn is similar to quartz monzonite in terms of TiO_2 contents, whereas garnet skarn spans the complete range from marble to quartz monzonite (Fig. 7a).

In general, garnet and epidote skarns are characterized by higher Al_2O_3 and lower MgO contents than garnet–diopside and diopside skarns (Fig. 7b, e), consistent with the relative abundance of garnet, epidote, and diopside in these skarn varieties. Garnet skarn has similar Al_2O_3, MgO, and LOI contents to quartz monzonite, but its CaO and K_2O contents are more similar to the marbles (Fig. 7b–f). The Fe_2O_3, MnO, and P_2O_5 contents of the skarns are greater than in the marbles and quartz monzonite (Fig. 7g–i).

Quartz monzonite is characterized by higher concentrations of the large ion lithophile elements (LILEs; e.g., Rb, Sr), high field strength elements (HFSEs; e.g., Zr, Nb), and Th than the marbles (Fig. 7j–n). Most of the skarns have similar Rb contents to the marbles (Fig. 7j), but are characterized by highly variable Sr contents (Fig. 7k). Notably, the Sr content in epidote skarn is almost 2000 ppm, which is approximately twice the concentration as in the quartz monzonite (Appendix Table A). Similar to Sr, the Zr, Nb, Th, and REE + Y contents of the different types of skarns are highly variable compared to the limited variability

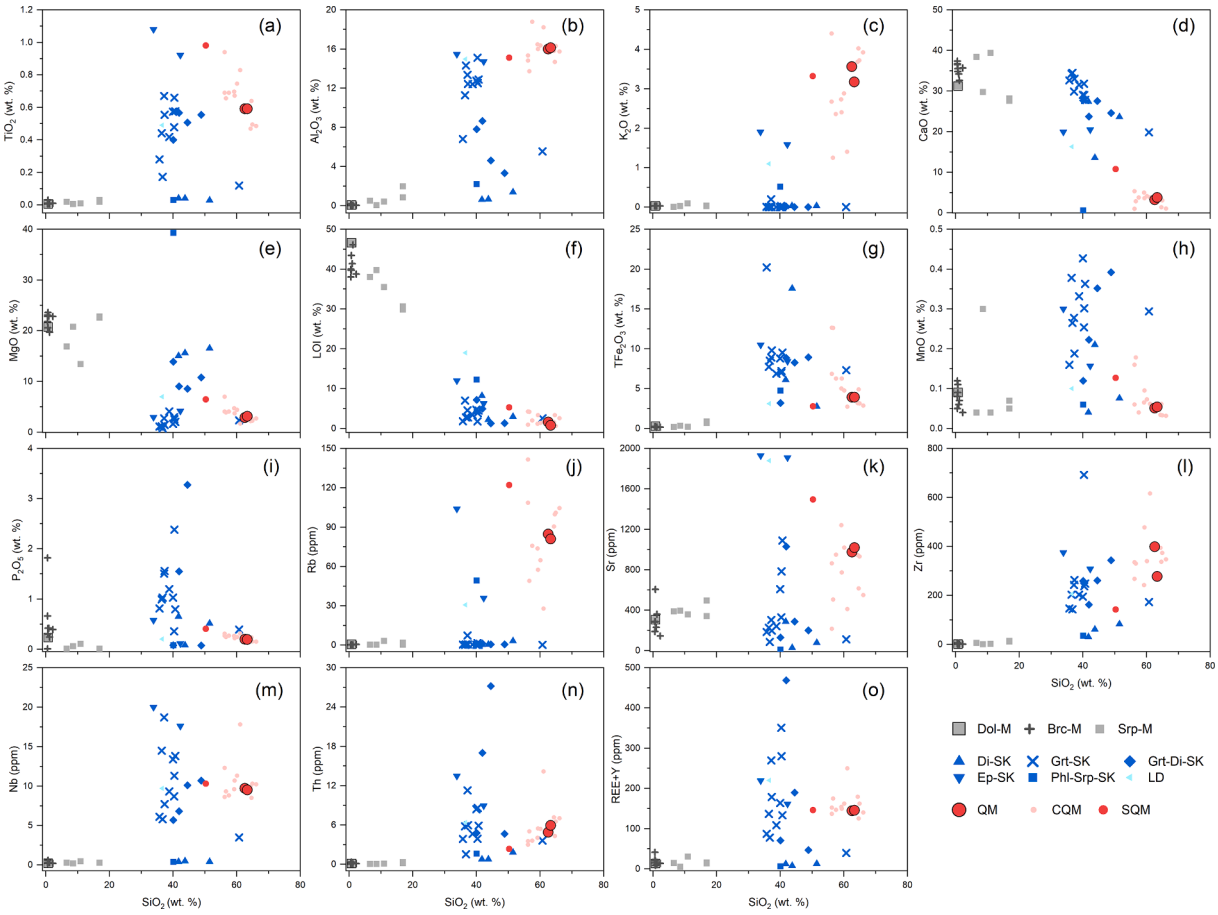

Fig. 7. Bivariate diagrams for selected elements versus SiO_2 contents in marbles, skarns, and quartz monzonite from the Yeshan Fe deposit. Dol-M = dolomite marble, Brc-M = brucite marble, Srp-M = serpentinized marble, Di-SK = diopside skarn, Grt-SK = garnet skarn, Grt-Di-SK = garnet–diopside skarn, Ep-SK = epidote skarn, Phl-Srp-SK = phlogopite–serpentine skarn, LD = loose debris at the contact zone, QM = quartz monzonite, CQM = chloritized quartz monzonite, SQM = skarn-altered quartz monzonite.

observed in the quartz monzonite and marbles (Fig. 7l–o).

6. Discussion

6.1. Skarn classification

Skarns developed at Yeshan are metasomatically zoned, with a pyroxene-rich assemblage proximal to the carbonate wall rock and a garnet-rich assemblage distal to the carbonate wall rock (Fig. 5), similar to other skarns in the world (e.g., Chang et al., 2019; Einaudi et al., 1981; Zharikov, 1970; Leng et al., 2021). This zonation pattern has been explained by the varying migration capability among elements during magma-derived fluid unidirectional infiltrated into the wall rock and the distance of Si transferring is larger than Al (Korzhinskii, 1959, 1970). It is worth noting that skarn zonation occurring as intrusion-pyroxene skarn-garnet skarn-marble has been recently emphasized (e.g., Soloviev et al., 2021; Soloviev et al., 2022). This skarn zonation is opposite to that developed at Yeshan, and may result from counter-infiltration processes (Zharikov, 1970).

Given the absolute immobile elements are difficult to constrain, the transfer variation among elements represented by the element ratios may offer the potential to characterize the skarn developed into different protoliths at Yeshan. The rationale is shown below. Without any specific knowledge about the skarn evolutionary stages, the zonation pattern at Yeshan can be reconciled with a simple fluid flow process (Meinert et al., 2005). Aluminum, Si, and other elements, such as Fe and Ti, in fluids would be sequestered into skarn minerals (e.g., garnet and pyroxene) during skarn alteration of carbonate wall rock at Yeshan. Similar to Al, Ti also has a lower mobility than Si in fluids (Rollinson, 1993). Aluminum and Ti are more compatible in garnet crystal structure than pyroxene (Deer et al., 1978, Deer et al., 1982); the proportion of Al and Ti in fluids decreased to a greater extent than that of Si- during garnet formation. Based on material balance theory (Hofmann, 1972), it may be, therefore, reasonable to expect that with increasing distance from the intrusion–carbonate contact zone, the SiO_2/Al_2O_3 and SiO_2/TiO_2 ratio in the magma-derived fluid while migrating into the carbonate wall rock would increase.

It is critical to compare the solubility of a component to its original abundance in the rock (i.e., relative solubility index, RSI); the higher the abundance of a particular element in a rock, the higher the fluid/rock ratios required to alter it (Leitch and Lentz, 1994). Due to the negligible SiO_2, Al_2O_3, and TiO_2 contents of the carbonate wall rock at Yeshan (Appendix Table A), the variable SiO_2/Al_2O_3 and SiO_2/TiO_2 signatures of the magma-derived fluids could be fingerprinted by skarns formed from the carbonate wall rock.

Experimental studies show that the partition coefficients (D) of Si, Al, and Ti between fluids and melts range from 0.0005 to 0.01 in the magmatic-hydrothermal systems ($P < 0.3$GPa, Keppler, 1996; Reed et al., 2000), and the D values of Si are significantly higher than Al and Ti. These results suggest that 1) the concentrations of Si, Al, and Ti in the magma-derived fluid are at least two orders of magnitude lower than these of magmatic rocks, assuming that the residual melt composition after fluid exsolution is approximately equal to that of intrusion at the Yeshan Fe deposit; and 2) the SiO_2/Al_2O_3 and SiO_2/TiO_2 ratios in the

magma-derived fluid are higher than these of intrusion. Considering no Si-Ti-Al-bearing strata, except the cogenetic intrusion, exists in the Xiaomiaochen area at Yeshan (Fig. 4a), the Si, Al, and Ti contents of magmatic fluids may not be successively enriched by extensive fluid/rock interactions, although the recent results of experimental studies and elemental analysis of fluid inclusions support that argument that these elements, particularly Ti traditionally considered as fluid-immobile (Rollinson, 1993), could have high contents (100 – 1000 ppm) in the magmatic fluids at high temperature and high salinity (Chen et al., 2019; Mysen, 2019; Rapp et al., 2010). Moreover, the concentrations of Si, Al, and Ti in the magma-derived fluids are roughly calculated to be 3000 ppm, 42 ppm, and 18 ppm, respectively, at the Yeshan Fe deposit, through multiplying these elemental contents of the intrusion (Appendix Table A) and the relative D values between fluids and melts. The D values are 0.01 and 0.0005 for Si and Al, respectively, at 800 °C and 2.0 kbar with fluids of 1.1 m Cl^- (Reed et al., 2000). The D value for Ti is approximately 0.005 at 1040 °C and 3.0 kbar with fluids of 5.0 m Cl^- (Keppler, 1996). It is worth noting that geochemical data are compositional data, which are traditionally defined as constrained data and carry relative rather than absolute information (Aitchison, 1986). Thus, elemental ratios are indeed the robust representation of the compositional properties of varying lithological units at the Yeshan Fe deposit. Given the low Si, Al, and Ti contents in the magmatic fluids discussed above, the SiO_2/Al_2O_3 and SiO_2/TiO_2 ratios of the igneous rocks would not be significantly modified by its cogenetic crystallized magma-derived fluid during skarn formation at Yeshan. Taken together, the variability in SiO_2/Al_2O_3 and SiO_2/TiO_2 ratio should be able to distinguish endoskarns from exoskarns in the Yeshan skarn system, with endoskarns being characterized by lower overall SiO_2/TiO_2 and SiO_2/Al_2O_3 ratios than exoskarns.

Given the low migration capability of Al and Ti compared to Si in hydrothermal fluids on a large transport scale (>20 m), their concentrations in distal skarns may be very low, resulting in anomalously high SiO_2/Al_2O_3 and SiO_2/TiO_2 ratios. For convenience, the natural logarithm of both ratios is used to gauge the mobility difference among Si, Al, and Ti during the infiltration of magma-derived fluid into the carbonate wall rocks. Fig. 8 schematically illustrates the theoretical basis for classifying endoskarn and exoskarn using $\ln(SiO_2/Al_2O_3)$ and $\ln(SiO_2/TiO_2)$ at Yeshan. It should be noted that the variations in SiO_2/Al_2O_3 and SiO_2/TiO_2 ratio may not be suitable for discriminating skarns formed proximal to the contact zone between the intrusion and the carbonate wall rock (i.e., garnet–pyroxene skarns); this topic will be discussed separately.

Using the framework of Fig. 8, two diopside skarn samples (ZK302-240 and ZK302-250) that are proximal to marbles have higher $\ln(SiO_2/Al_2O_3)$ and $\ln(SiO_2/TiO_2)$ values than the garnet skarn samples and are classified as exoskarns (Fig. 9d, e). The $\ln(SiO_2/Al_2O_3)$ values of two garnet skarn samples (ZK302-270 and ZK302-290) are distinctly higher than those in the igneous rocks, but lower than those in the diopside skarns (Fig. 9e). These garnet skarn samples match in the $\ln(SiO_2/Al_2O_3)$ and $\ln(SiO_2/TiO_2)$ values well the proximal garnet skarns developed at the wall rocks in Fig. 8 and are considered exoskarns. The remaining garnet skarn samples with $\ln(SiO_2/Al_2O_3)$ values similar to the igneous rocks are classified as endoskarns. However, one garnet skarn sample ZK302-450 has a $\ln(SiO_2/TiO_2)$ value closer to these of proximal garnet skarns (Fig. 9d); the final judgment of this sample would require other geochemical indexes.

Four garnet–diopside skarn samples (ZK302-471, ZK302-471.5, ZK302-510, and ZK302-686) have higher $\ln(SiO_2/Al_2O_3)$ and comparable $\ln(SiO_2/TiO_2)$ values to the igneous rocks (Fig. 9d, e). These samples characterized by low garnet/diopside abundance ratios commonly form in relatively reduced environments, such as the igneous–wall rock contact zone where the effects of the oxidized magma may be lessened or completely masked by very reduced carbonate wall rocks (Meinert et al., 2005). Accordingly, due to the relatively small migration distance, the difference in mobility among Si, Al, and Ti may not be manifested at the contact zone. Again, other geochemical indices are, therefore, required to classify the garnet–diopside skarn as either endo- or exoskarn.

The REE + Y content of the igneous rocks is significantly higher than the marbles at Yeshan (Fig. 7o). Based on the partition coefficient of REE between fluids and melts (Reed et al., 2000; Wen et al., 2020), the REE + Y contents in the exsolving magma-derived fluids are crudely calculated to be about 4.5 ppm following the similar calculation procedure for Si, Ti, and Al in fluids. The REE + Y content of skarns formed at the contact zone (e.g., garnet–diopside skarn) is expected to be more similar to their protolith. Accordingly, garnet–diopside skarn samples ZK302-471.5 and ZK302-510, which are characterized by REE + Y contents similar to or greater than the igneous rocks, likely formed from the igneous rocks and are classified as endoskarns (Fig. 9f). The other two garnet–diopside skarn samples (ZK302-471 and ZK302-686) have REE + Y contents that are more similar to the marbles and are classified as exoskarns (Fig. 9f). The classification of these garnet–diopside skarn samples at Yeshan as exoskarns suggests that TiO_2 may be able to be transferred in significant quantities into the wall rocks along with SiO_2 and Al_2O_3 on a small transport scale (<5 m); this is supported by the ilmenite mineralization observed in the garnet–diopside exoskarn along the diorite–marble contact (Altunbey and Sagiroglu, 2003). The garnet skarn sample ZK302-450 exhibits the REE + Y content similar to the marbles (Fig. 9f), and is more likely to form into the carbonate wall rock.

Two epidote skarn samples (ZK302-530 and ZK302-550) have ln (SiO_2/Al_2O_3), $\ln(SiO_2/TiO_2)$ values, and REE + Y contents comparable to the igneous rocks, suggesting that their protoliths are likely the igneous rocks; they are, therefore, classified as endoskarns. The

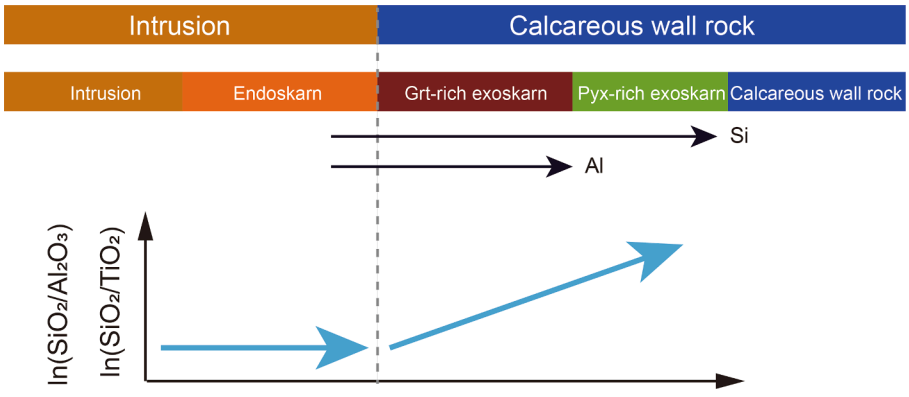

Fig. 8. Idealized skarn zonation pattern modified after Einaudi et al., (1981) and Zharikov, (1970) illustrating a general variation of whole-rock $\ln(SiO_2/Al_2O_3)$ and $\ln(SiO_2/TiO_2)$ from intrusion, endoskarn, and exoskarn at Yeshan. The black arrows show the direction and distance in which Si and Al from the magma-derived fluid transfer into the wall rock. Noting that the horizontal widths of the skarn zones are artificially scaled.

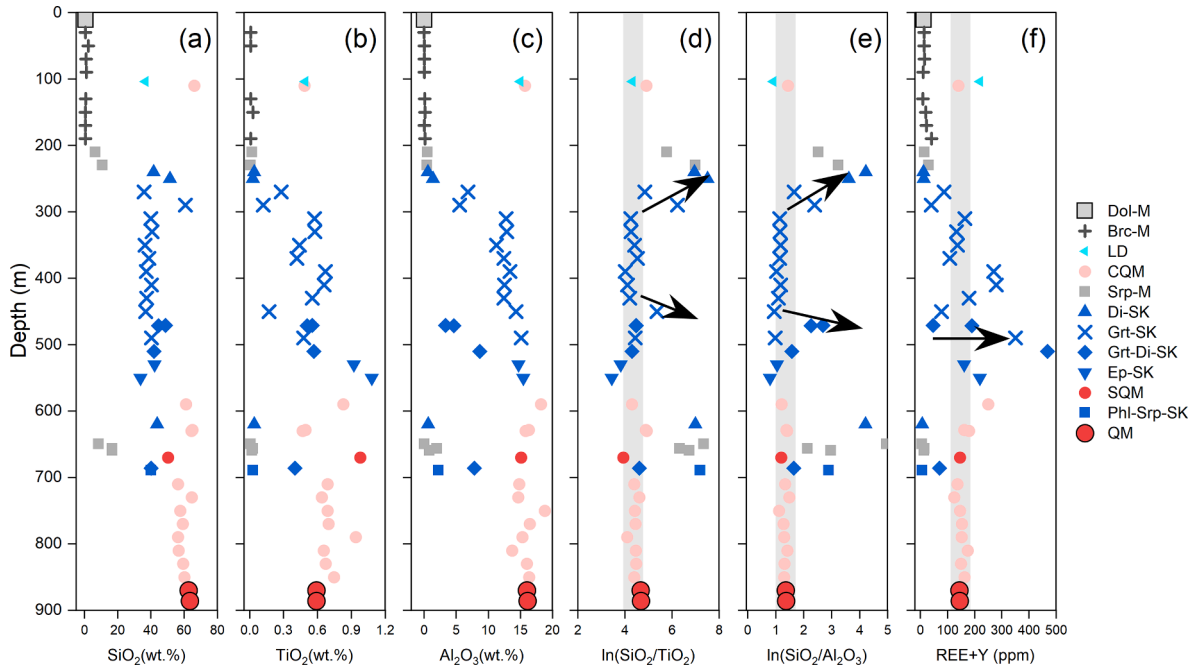

Fig. 9. Down-hole variation diagrams illustrating the change in bulk-rock (**a**) SiO_2, (**b**) TiO_2, (**c**) Al_2O_3, (**d**) SiO_2/TiO_2, (**e**) $ln(SiO_2/Al_2O_3)$, and (**f**) REE + Y contents along drill core ZK302. The grey bar represents the range of quartz monzonite and skarn-altered quartz monzonite. The $ln(SiO_2/Al_2O_3)$ and $ln(SiO_2/TiO_2)$ values are used to identify the protoliths of diopside skarn and garnet skarn. The REE + Y contents are used to identify the garnet–diopside skarns. All data are presented in Appendix Table A. Dol-M = dolomite marble, Brc-M = brucite marble, LD = loose debris at the contact zone, CQM = chloritized quartz monzonite, Srp-M = serpentinized marble, Di-SK = diopside skarn, Grt-SK = garnet skarn, Grt-Di-SK = garnet–diopside skarn, Ep-SK = epidote skarn, SQM = skarn-altered quartz monzonite, Phl-Srp-SK = phlogopite–serpentine skarn, QM = quartz monzonite.

classification of all skarns in this study is shown in Appendix Table A. In summary, endoskarn is more abundant than exoskarn at Yeshan.

6.2. Element mobility during endoskarn formation

Based on the extent of alteration and mineral paragenesis, two representative endoskarn samples (ZK302-670 and ZK302-390) from the Yeshan Fe deposit were selected to constrain mass transfer during endoskarn formation. Samples ZK302-886 and ZK302-870 are unaltered igneous rocks and chosen as the endoskarn protolith.

Sample ZK302-670 characterized by the coexistence of diopside and igneous biotite (Fig. 5k, 6f-g) represents the earliest stage of alteration of the igneous rocks. Nearly half of the feldspar crystals were replaced by diopside, with no new Al-bearing minerals having formed (Fig. 5k); Al_2O_3 was, therefore, likely lost to the fluids during this early stage of skarn alteration. The slope of the isocon line defined by P_2O_5, TiO_2, Ba, Sc, and Cr is 1.66 (Fig. 10a), indicating a total mass loss of 40% (Appendix Table B). MgO, CaO, MnO, and volatiles (expressed as LOI) were added, whereas SiO_2, Al_2O_3, Fe_2O_3, Na_2O, and K_2O were removed from the igneous rock during this stage of skarn formation. The added MgO, CaO, and MnO were taken up by newly formed diopside, whereas the lost SiO_2, Al_2O_3, Na_2O, and K_2O may be related to the partial destruction of feldspar. These lost elements could have migrated into the wall rock and precipitated Al–Si–bearing minerals, such as garnet, diopside, and spinel (e.g., sample ZK302-686; Fig. 5l, 6 h). The increased sericitization, chloritization, and carbonation of the igneous rocks is likely a result of the addition of volatiles.

Trace elements were mobilized at this stage of alteration, with most having been removed from the igneous rock. Zirconium, Hf, Th, and U exhibit similar losses (Fig. 10a), which may be due to the dissolution of

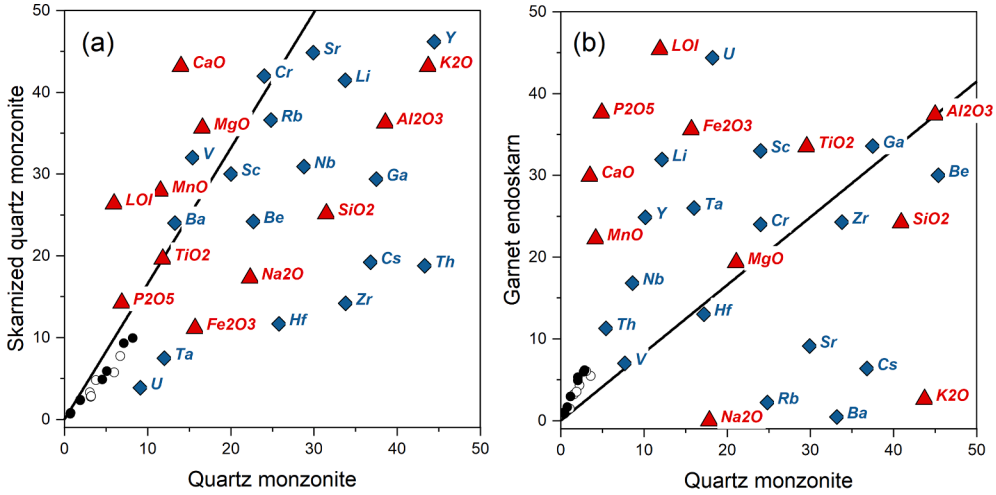

Fig. 10. Isocon diagrams used to characterize element mobility during skarn alteration of quartz monzonite in the Yeshan Fe deposit. Element concentrations are arbitrarily scaled to avoid stacking. The original composition of quartz monzonite used for calculation is defined by the average of samples ZK302-870 and ZK302-886. The black line represents the isocon. Elements plotting above the isocon indicate enrichment/gains, whereas those below indicate depletion/losses. Open and solid circles denote the light rare earth elements (LREE) and heavy rare earth elements (HREE), respectively. (**a**) Skarn-altered quartz monzonite (ZK302-670). (**b**) Garnet skarn (ZK302-390).

zircon during the skarn alteration or the zircon heterogeneity in the igneous protolith.

Sample ZK302-390 is chosen as an example to illustrate element mobility during garnet endoskarn formation as it is characterized by a high abundance of garnet (~80% in volume) and relatively low abundance of retrograde minerals, particularly epidote (Fig. 5f), simplifying the interpretation of element mobility during the prograde skarn stage.

In contrast to sample ZK02-670, skarn minerals in garnet endoskarn are Al-bearing minerals (garnet). The Al_2O_3-constant isocon is chosen and has a slope value of 0.83 (Fig. 10b), which corresponds to a 20% increase in the total mass of the rock (Appendix Table B). In this scenario, the formation of garnet endoskarn resulted in a minor gain in MgO and a moderate gain in TiO_2 (Fig. 10b). The soluble of TiO_2 in hydrothermal fluids has been experimentally demonstrated (Rapp et al., 2010).

CaO, MnO, Fe_2O_3, P_2O_5, and volatiles show significantly gained during garnet endoskarn formation, and K_2O, Na_2O, and LILEs (e.g., Rb, Cs, Ba, and Sr) lost. Nb, Ta, and Th were added during this stage of skarn formation (Fig. 10b). Experimental studies have demonstrated that the chloride complexes are not important for mobilizing Nb and Ta in hydrothermal fluids (Kotova, 2015; Akinfiev et al., 2020). The stability of Th-chloride complexes at temperatures above 250°C is poorly understood (Nisbet et al., 2018). Other ligands (e.g., fluorine, phosphate, hydroxide, carbonate) should be, therefore, considered in the future for the transportation of Nb, Ta, and Th at Yeshan.

6.3. Element mobility during exoskarn formation

Carbonate is sensitive to elemental mobility during exoskarn formation because of its relatively simple chemical composition. Sample ZK302-11 is chosen as the protolith for the exoskarns as it has the greatest abundance of dolomite and is least altered (i.e., the lowest proportion of brucite). Given the relatively simple mineralogy, samples ZK302-240 (~90% diopside with subordinate magnetite and apatite) and ZK302-270 (~90% garnet and ~10% calcite) are chosen to evaluate the geochemical changes that accompanied exoskarn formation.

In the isocon diagram for diopside exoskarn formation, the isocon line defined by CaO, V, Li, Cs, Sr, Y, and rare earth elements has a slope of 0.87, suggesting a mass gain of 14%. The formation of diopside exoskarn resulted in a significant increase in SiO_2 and Fe_2O_3, and a significant loss of volatiles; CaO and MgO contents were not significantly affected (Fig. 11a). The addition of SiO_2 and Fe_2O_3 is consistent with the presence of diopside and magnetite.

TiO_2, Zr, and Th were gained during this stage of exoskarn formation (Appendix Table A; Fig. 11a), which is consistent with the presence of ilmenite and Th–Zr-bearing minerals (Fig. 6a). The water/rock ratio for diopside exoskarn formation is calculated to be approximately 540 based on a SiO_2 concentration in the hydrothermal fluid of 20 mmol per kilogram H_2O (Li et al., 2020). SiO_2, Al_2O_3, TiO_2, and Fe_2O_3, which are required for garnet formation, were added during the formation of garnet exoskarn, whereas MgO and volatiles were significantly lost. Rare earth elements, Y, Nb, U, and V compatible in the crystal structure of garnet, were, likely sequestered into garnet. Lithium, however, is highly incompatible into garnet (Brenan et al., 1998). Considering the low Li content of sample ZK302-270, it is inferred that the Li content of the wall rocks was not significantly modified by alteration. Lithium is, therefore, used as a reference framework to constrain mass transfer during garnet exoskarn formation, which corresponds to a total mass loss of 47% (Fig. 11b; Appendix Table C). Given the negligible concentration of Nb, Ta, Th, and Ga in the wall rocks (Appendix Table A), the addition of these elements in the garnet exoskarn provides robust evidence for their mobility in fluids.

Based on the solubility of microcline–muscovite–quartz and albite–paragonite–quartz (Woodland and Walther, 1987; Walther and Woodland, 1993), the calculated water/rock ratio for garnet exoskarn formation is approximately 560. This value is comparable with the estimated water/rock ratio for grandite exoskarn formation at the Mochito Zn deposit (Williams-Jones et al., 2010).

7. Conclusions

The Yeshan Fe deposit is a typical skarn Fe deposit in Eastern China. Alteration and mineralization at Yeshan are associated with the emplacement of Early Cretaceous quartz monzonite into Sinian dolostone. No textures of protoliths preserve in skarns. To develop a lithogeochemical technique for discriminating between endo- and exoskarns, and quantifying element mobility at Yeshan, a drill hole through the Yeshan Fe deposit was targeted that intersects the complete stratigraphic sequence of the skarn system. Underpinned by the skarn zonation model, a criterion that the SiO_2/Al_2O_3 and SiO_2/TiO_2 ratios in exoskarn are higher than endoskarn has been proposed and used to characterize the protolith of varying skarns formed far from the contact zone at Yeshan. For skarns formed near the contact zone (e.g., garnet-diopside skarn), their protoliths could be identified using whole-rock REE + Y contents, given the significant difference in REE + Y content between the igneous and the carbonate wall rocks. Classification results

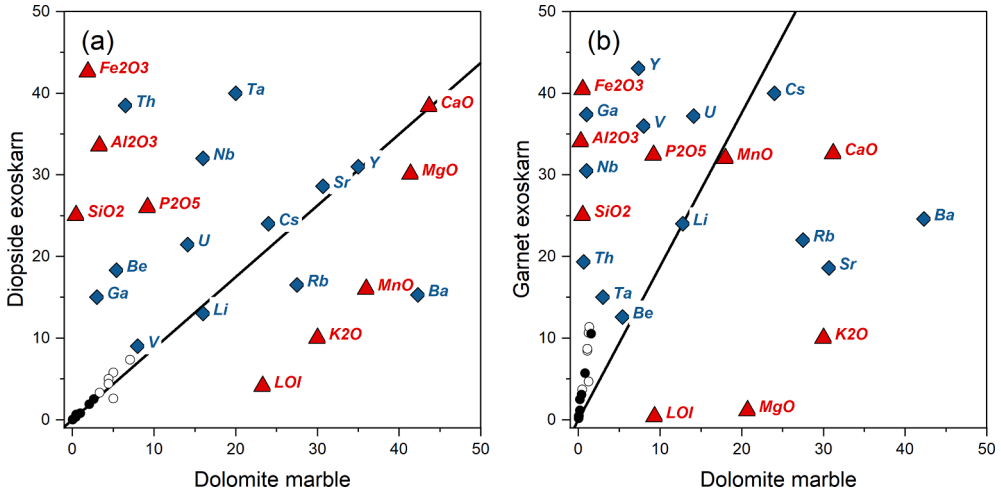

Fig. 11. Isocon diagrams used to characterize element mobility during exoskarn formation in the Yeshan Fe deposit. Dolomite marble (ZK302-11) is selected as the protolith of the exoskarns. The black solid lines represent the isocon Open and solid circles denote the light rare earth elements (LREE) and heavy rare earth elements (HREE), respectively. (**a**) Diopside exoskarn (ZK302-240). (**b**) Garnet exoskarn (ZK302-270).

show that endoskarns are more abundant than exoskarns at Yeshan. Isocon analysis suggests that almost all elements could be mobile at the Yeshan Fe deposit.

Declaration of Competing Interest

The authors declare that they have no known competing financial interests or personal relationships that could have appeared to influence the work reported in this paper.

Acknowledgements

This work is funded by the National Natural Science Foundation of China (Project No. 41622301) to Weiqiang Li. Zhaoshan Chang is greatly appreciated for discussion about the classification of endoskarn and exoskarn. Insightful reviews by two anonymous reviewers have greatly improved this manuscript. We thank Tianyi Huang, Jun Chen, and Hui Wang for their help with field investigations.

Appendix A. Supplementary data

Supplementary data to this article can be found online at https://doi.org/10.1016/j.oregeorev.2022.104909.

References

Aitchison, J., 1986. The Statistical Analysis of Compositional Data. Monographs on Statistics and Applied ProbabilityChapman and Hall Ltd. (Reprinted 2003 with additional material by The Blackburn Press), London (UK) (416 pp.).
Akinfiev, N.N., Korzhinskaya, V.S., Kotova, N.P., Redkin, A.F., Zotov, A.V., 2020. Niobium and tantalum in hydrothermal fluids: Thermodynamic description of hydroxide and hydroxofluoride complexes. Geochim. Cosmochim. Acta. 280, 102–115.
Altunbey, M., Sagiroglu, A., 2003. Skarn-type ilmenite mineralization of the Tuzbaşi-Tunceli region, eastern Turkey. J. Asian Earth Sci. 21 (5), 481–488.
Brenan, J.M., Ryerson, F.J., Shaw, H.F., 1998. The role of aqueous fluids in the slab-to-mantle transfer of boron, beryllium, and lithium during subduction: experiments and models. Geochim. Cosmochim. Acta. 62 (19-20), 3337–3347.
Chang, Y.F., Liu, X.P., Wu, Y.C., 1991. The Copper-Iron Belt of the Lower and Middle Reaches of the Changjiang River. Geological Publishing House, Beijing, p. 379 (in Chinese).
Chang, Z.S., Shu, Q.H., Meinert, L.D., 2019. Skarn deposits of China. SEG Special Publ. 22, 189–234.
Chen, J., Wang, H., Wang, L.J., Guan, J.P., 2018. Petrogenesis of Jinniu rock mass in Chuzhou area: melting of delaminated lower crust or mixing of crust and mantle. Geol. China. 45, 110–128 (in Chinese with English abstract).
Chen, P., Zeng, Q., Zhou, T., Wang, Y., Yu, B., Chen, J., 2019. Evolution of fluids in the Dasuji porphyry Mo deposit on the northern margin of the North China Craton: constraints from microthermometric and LA–ICP–MS analyses of fluid inclusions. Ore Geol. Rev. 104, 26–45.
Chen, Z.H., Zhao, L., Li, Y.N., 2017. Zircon U-Pb ages of ore-free intrusions in the ningzhen metallogenic district of the middle-Cambrian Yangtze River metallogenic belt and their geological significances. Bull. Mineral. Petrol. Geochem. 36, 171–178 (in Chinese with English abstract).
Deer, W.A., Howie, R.A., Zussman, J., 1982. Rock-forming minerals. 2nd edition. Orthosilicates, Volume 1A. Longman (917 pp.).
Deer, W.A., Howie, R.A., Zussman, J., 1978. Rock-forming minerals. 2nd edition. Single-chain Silicates vol. 2A. Longman (668 pp.).
Deng, J., Yang, X., Li, S., Gu, H., Mastoi, A.S., Sun, W., 2016. Partial melting of subducted paleo-Pacific plate during the early Cretaceous: constraint from adakitic rocks in the Shaxi porphyry Cu–Au deposit, Lower Yangtze River Belt. Lithos 262, 651–667.
Einaudi, M.T., Meinert, L.D., Newberry, R.J., 1981. Skarn deposits. Economic Geology 75th Anniversary Volume 317–391.
Fan, Y., Zhou, T.F., Yuan, F., Qian, C.C., Lu, S.M., Cooke, D., 2008. LA–ICP–MS zircon U-Pb ages of the A-type granites in the Lu–Zong (Lujiang–Zongyang) area and their geological significances. Acta Petrol. Sin. 24, 1715–1724 (in Chinese with English abstract).
Giere, R., 1990. Hydrothermal mobility of Ti, Zr and REE: examples from the Bergell and Adamello contact aureoles (Italy). Terra Nova 2, 60–67.
Grant, J.A., 1986. The isocon diagram—a simple solution to Gresens' equation for metasomatic alteration. Econ. Geol. 81, 1976–1982.
Hu, H., Li, J.W., Harlov, D.E., Lentz, D.R., McFarlane, C.R., Yang, Y.H., 2020. A genetic link between iron oxide-apatite and iron skarn mineralization in the Jinniu volcanic basin, Daye district, eastern China: evidence from magnetite geochemistry and multimineral U-Pb geochronology. Geol. Soc. Am. Bull. 132, 899–917.
Hofmann, A., 1972. Chromatographic theory of infiltration metasomatism and its application to feldspars. Am. J. Sci. 272 (1), 69–90.
Jiangsu Bureau Geological Mineral Resource, 1989. Memoir on Geology of Nanjing-Zhenjiang Mountains. Phoenix Science Press, Nanjing, p. 407 (in Chinese).
Keppler, H., 1996. Constraints from partitioning experiments on the composition of subduction-zone fluids. Nature 380 (6571), 237–240.
Korzhinskii, D.S., 1959. Physicochemical Basis of the Analysis of the Paragenesis of Minerals. Consultants Bureau, New York and Chapman & Hall, London, p. 142.
Korzhinskii, D.S., 1970. Theory of Metasomatic Zoning. Clarendon Press, Oxford, p. 162.
Kotova, N.P., 2015. Experimental study of Nb_2O_5 solubility in chloride solutions at 300–550 °C and 100 MPa. Exp. GeoSci. 21, 41–42.
Leitch, C.H.B., Lentz, D.R., 1994. The Gresens approach to mass balance constraints of alteration systems. Geol. Assoc. Canada Short Course Notes 11, 161–192.
Leng, Q.F., Tang, J.X., Zheng, W.B., Tang, P., Lin, B., 2021. Skarn mineral assemblage and zonation pattern in Jiama superlarge deposit, Tibet. Acta Geol. Sin. 95, 1–36 (in Chinese with English abstract).
Lentz, D.R., 2005. Mass-balance analysis of mineralized skarn systems: implications for replacement processes, carbonate mobility, and permeability evolution. In: Mao, J., Bierlein, F.P. (Eds.), Mineral Deposit Research: Meeting the Global Challenge. Springer Berlin Heidelberg, pp. 421–424.
Li, J.-W., Vasconcelos, P.M., Zhou, M.-F., Deng, X.-D., Cohen, B., Bi, S.-J., Zhao, X.-F., Selby, D., 2014. Longevity of magmatic-hydrothermal systems in the Daye Cu-Fe-Au district, eastern China with implications for mineral exploration. Ore Geol. Rev. 57, 375–392.
Li, W., Xie, G.Q., Mao, J.W., Zhu, Q.Q., Zheng J.H., 2019. Mineralogy, Fluid Inclusion, and Stable Isotope Studies of the Chengchao Deposit, Hubei Province, Eastern China: implications for the Formation of High-Grade Fe Skarn Deposits. Econ. Geol. 114, 325–352.
Li, X.-H., Klyukin, Y.I., Steele-MacInnis, M., Fan, H.-R., Yang, K.-F., Zoheir, B., 2020. Phase equilibria, thermodynamic properties, and solubility of quartz in saline-aqueous-carbonic fluids: application to orogenic and intrusion-related gold deposits. Geochim. Cosmochim. Acta 283, 201–221.
Li, Z.-X., Li, X.-H., 2007. Formation of the 1300-km-wide intracontinental orogen and postorogenic magmatic province in Mesozoic South China: a flat-slab subduction model. Geology 35 (2), 179. https://doi.org/10.1130/G23193A.110.1130/2007041.
Liang, S., Wei, J., Zhao, Z., Shi, W., 2018. The Cretaceous Huangdaoshan Cu-bearing intrusion in Chuzhou: petrogenesis and implications for the Cu mineralization in the middle–lower Yangtze River Valley Metallogenic Belt, eastern China. Ore Geol. Rev. 101, 900–918.
Ling, M.-X., Wang, F.-Y., Ding, X., Hu, Y.-H., Zhou, J.-B., Zartman, R.E., Yang, X.-Y., Sun, W., 2009. Cretaceous ridge subduction along the Lower Yangtze River belt, Eastern China. Econ. Geol. 104 (2), 303–321.
Mao, J., Pirajno, F., Cook, N., 2011a. Mesozoic metallogeny in East-China and corresponding geodynamic settings—an introduction to the special issue. Ore Geol. Rev. 43 (1), 1–7.
Mao, J., Xie, G., Duan, C., Pirajno, F., Ishiyama, D., Chen, Y., 2011b. A tectono-genetic model for porphyry-skarn-stratabound Cu-Au-Mo-Fe and magnetite-apatite deposits along the Middle-Lower Yangtze River Valley, eastern China. Ore Geol. Rev. 43 (1), 294–314.
Maydagán, L., Franchini, M., Impiccini, A., Lentz, D., 2016. Phyllosilicates geochemistry and distribution in the Altar porphyry Cu-(Au) deposit, Andes Cordillera of San Juan, Argentina: applications in exploration, geothermometry, and geometallurgy. J. Geochem. Explor. 167, 83–109.
Meinert, L.D., Dipple, G.M., Nicolescu, S., 2005. World skarn deposits. In: Hedenquist, J. W., Thompson, J.F.H., Goldfarb, R.J., Richards, J.P. (Eds.), Economic Geology 100th Anniversary Volume. Society of Economic Geologists, Littleton, CO, pp. 299–336.
Mrozek, S.A., Chang, Z.S., Spandler, C., Windle, S., Raraz, C., Paz, A., 2020. Classifying skarns and quantifying metasomatism at the Antamina deposit, Peru: insights from whole-rock geochemistry. Econ. Geol. 115, 177–188.
Mysen, B., 2019. Aqueous fluids as transport medium at high pressure and temperature: Ti^{4+} solubility, solution mechanisms, and fluid composition. Chem. Geol. 505, 57–65.
Ningwu Research Group, 1978. Ningwu Porphyrite Iron Ores. Geological Publishing House, Beijing, pp. 1–196 (in Chinese).
Nisbet, H., Migdisov, A.A., Xu, H., Guo, X., Van Hinsberg, V., Williams-Jones, A.E., Boukhalfa, H., Roback, R., 2018. An experimental study of the solubility and speciation of thorium in chloride-bearing aqueous solutions at temperatures up to 250 °C. Geochim. Cosmochim. Acta. 239, 363–373.
Ordóñez-Calderón, J.C., Gelcich, S., Fiaz, F., 2017. Lithogeochemistry and chemostratigraphy of the Rosemont Cu-Mo-Ag skarn deposit, SE Tucson Arizona: a simplicial geometry approach. J. Geochem. Explor. 180, 35–51.
Pan, Y.M., Dong, P., 1999. The Lower Changjiang (Yangzi/Yangtze River) metallogenic belt, east China: intrusion- and wall rock-hosted Cu-Fe-Au, Mo, Zn, Pb, Ag deposits. Ore Geol. Rev. 15, 177–242.
Peccerillo, A., Taylor, S.R., 1976. Geochemistry of Eocene calc-alkaline volcanic rocks from the Kastamonu area, northern Turkey. Contrib. Mineral. Petrol. 58 (1), 63–81.
Pirajno, F., 2013. The Geology and Tectonic Settings of China's Mineral Deposits. Springer, Dordrecht, p. 679.
Rapp, J.F., Klemme, S., Butler, I.B., Harley, S.L., 2010. Extremely high solubility of rutile in chloride and fluoride-bearing metamorphic fluids: an experimental investigation. Geology. 38, 323–326.
Reed, M.J., Candela, P.A., Piccoli, P.M., 2000. The distribution of rare earth elements between monzogranitic melt and the aqueous volatile phase in experimental investigations at 800°C and 200 MPa. Contrib. Mineral. Petrol. 140 (2), 251–262.
Rollinson, H.R., 1993. Using Geochemical Data: Evaluation, Presentation, Interpretation. Longman Scientific and Technical Press, pp. 306–308.
Soloviev, S.G., Kryazhev, S.G., Shapovalenko, V.N., Dvurechenskaya, S.S., Semenova, D. V., Kalinin, Y.A., Voskresensky, K.I., Sidorova, N.V., 2021. The Glafirinskoe and

related skarn Cu-Au-W-Mo deposits in the Northern Altai, SW Siberia, Russia: Geology, igneous geochemistry, zircon U-Pb geochronology, mineralization, and fluid inclusion characteristics. Ore Geol. Rev. 138, 104382. https://doi.org/10.1016/j.oregeorev.2021.104382.

Soloviev, S.G., Kryazhev, S.G., Semenova, D.V., Kalinin, Y.A., Dvurechenskaya, S.S., Sidorova, N.V., 2022. Geology, mineralization, igneous geochemistry, and zircon U-Pb geochronology of the Early Paleozoic shoshonite-related Julia skarn deposit, SW Siberia, Russia: toward a diversity of Cu-Au-Mo skarn to porphyry mineralization in the Altai-Sayan orogenic system. Ore Geol. Rev. 142, 104706. https://doi.org/10.1016/j.oregeorev.2022.104706.

Sun, Q., Zhao, M., Zhang, W.L., 2017. Formation mechanism of the yeshan skarn-type boron deposit, Nanjing, Jiangsu Province: constraints from borate minerals. Geol. J. China Univ. 23, 417–430 (in Chinese with English abstract).

Sun, Y., Ma, C., Liu, Y., 2013. The latest Yanshanian magmatic and metallogenic events in the middle-lower Yangtze River belt: evidence from the Ningzhen region. Chin. Sci. Bull. 58 (34), 4308–4318.

Walther, J.V., Woodland, A.B., 1993. Experimental determination and interpretation of the solubility of the assemblage microcline, muscovite, and quartz in supercritical H2O. Geochim. Cosmochim. Acta. 57 (11), 2431–2437.

Wen, G., Li, J.-W., Hofstra, A.H., Koenig, A.E., Cui, B.-Z., 2020. Textures and compositions of clinopyroxene in an Fe skarn with implications for ore-fluid evolution and mineral-fluid REE partitioning. Geochim. Cosmochim. Acta 290, 104–123.

Whitney, D.L., Evans, B.W., 2010. Abbreviations for names of rock-forming minerals. Am. Mineral. 95 (1), 185–187.

Williams-Jones, A.E., Samson, I.M., Ault, K.M., Gagnon, J.E., Fryer, B.J., 2010. The genesis of distal zinc skarns: Evidence from the Mochito deposit. Honduras. Econ. Geol. 105 (8), 1411–1440.

Woodland, A.B., Walther, J.V., 1987. Experimental determination of the solubility of the assemblage paragonite, albite, and quartz in supercritical H2O. Geochim. Cosmochim. Acta. 51 (2), 365–372.

Xiao, Q., Zhou, T., Hollings, P., Wang, S., Liu, J., Yang, Q., Yuan, F., 2021. Mineral and whole-rock chemistry of the Chating porphyry Cu–Au deposit related intrusions in the Middle-Lower Yangtze River Belt, Eastern China: Implications for magma evolution and mineralization. Lithos 380-381, 105881. https://doi.org/10.1016/j.lithos.2020.105881.

Xie, G., Mao, J., Zhao, H., Wei, K., Jin, S., Pan, H., Ke, Y., 2011. Timing of skarn deposit formation of the Tonglushan ore district, southeastern Hubei province, Middle-Lower Yangtze River Valley metallogenic belt and its implications. Ore Geol. Rev. 43 (1), 62–77.

Xie, G., Mao, J., Zhao, H., Duan, C., Yao, L., 2012. Zircon U-Pb and phlogopite ^{40}Ar-^{39}Ar age of the Chengchao and Jinshandian skarn Fe deposits, southeast Hubei province, Middle-Lower Yangtze River Valley metallogenic belt, China. Mineral. Deposita. 47 (6), 633–652.

Yu, J.-J., Wang, T.-Z., Che, L.-R., Lu, B.-C., 2016. Geological, geochronological, and H-O isotopic constraints on the genesis of the Tongjing Cu–Au deposit in the Ningwu basin, east China. Ore Geol. Rev. 78, 346–360.

Zeng, J.N., Li, J.W., Chen, J.H., Lu, J.P., 2013. SHRMP Zircon U-Pb dating of Anjishan intrusive rocks in Ningzhen district, Jiangsu, and its geological significance. Earth Sci. 38 (1), 57–67 (in Chinese with English abstract).

Zhai, Y.S., Yao, S.Z., Lin, X.D., Zhou, X.N., Wan, T.F., Jin, F.Q., Zhou, Z.G., 1992. Fe–Cu–Au Metallogeny of the Middle-Lower Changjiang Region. Geological Publishing House, Beijing, p. 235 (in Chinese).

Zhang, M.C., Chen, R.Y., Ye, T.Z., Yao, L., Li, J.C., Li, Y.S., He, X., Sun, H.R., Liu, S.Y., 2018. Zircon U—Pb Dating and Hf Isotopic Compositions of the Anjishan Granodiorite Porphyry and Weigang Granodiorite in the Ningzhen Ore Cluster Area and Their Geological Implications. Acta Geol. Sin. 92, 2248–2268.

Zharikov V.A., 1970. Skarns. Int. Geol. Rev 12, 541–559, 619–647, 720–775.

Zhou, T., Fan, Y.u., Yuan, F., Zhang, L., Qian, B., Ma, L., Yang, X., 2013. Geology and geochronology of magnetite–apatite deposits in the Ning–Wu volcanic basin, eastern China. J. Asian Earth Sci. 66, 90–107.

Zhou, T.F., Wu, M.G., Yu, F., Chao, D., Feng, Y., Zhang, L.J., Liu, J., Pirajno, F., Cooke, D. R., 2011. Geological, geochemical characteristics and isotope systematics of the Longqiao iron deposit in the Lu-Zong volcanosedimentary basin, Middle-Lower Yangtze River Valley, eastern China. Ore Geol. Rev. 43, 154–169.

Zhou, X.M., Li, W.X., 2000. Origin of Late Mesozoic igneous rocks in Southeastern China: implications for lithosphere subduction and underplating of mafic magmas. Tectonophysics 326 (3-4), 269–287.

Zi, F., Wang, Q., Liu, X.H., Qiu, H.N., 2011. Geochronology and Geochemistry of the Yeshan and Shanlichen Adakitic Intrusive Rocks in the Eastern Yangtze Block: Petrogenesis and Its Geodynamic Implications. Acta Mineral. Sinica. 31, 185–200 (in Chinese with English abstract).